Textile & Leather Review

ISSN 2623-6281| www.tlr-journal.com | 10.31881/TLR

Wavelet-Enhanced Active Disturbance Rejection Control for PMSM in Low-Speed Textile Processing

Xiaoyan Han

How to cite: Han X. Wavelet-Enhanced Active Disturbance Rejection Control for PMSM in Low-Speed Textile Processing. Textile & Leather Review. 2026; 9:748-776. https://doi.org/10.31881/TLR.2026.748

How to link: https://doi.org/10.31881/TLR.2026.748

Published: 31 March 2026

Wavelet-Enhanced Active Disturbance Rejection Control for PMSM in Low-Speed Textile Processing

Xiaoyan Han

Intelligent Manufacturing College, Zhengzhou University of Economics and Business, Zhengzhou 451191, Henan, China

*htdmhxy@163.com

Article

https://doi.org/10.31881/TLR.2026.748

Received 30 September 2025; Accepted 30 October 2025; Published 31 March 2026

ABSTRACT

This paper addresses the speed fluctuation problem of permanent magnet synchronous machines (PMSMs) under low-speed conditions in high-precision fabric and leather processing. An improved Active Disturbance Rejection Control (ADRC) algorithm is proposed. Based on a tracking differentiator-extended state observer-nonlinear state error feedback law structure, a wavelet packet analysis-enhanced adaptive extended state observer (AESO) is used to estimate and compensate for composite disturbances. A hyperbolic tangent nonlinear feedback law is applied to suppress chattering, and a recursive least squares (RLS) algorithm is employed for online identification and feedforward compensation of time-varying parameters. The integral absolute error (IAE) is reduced to 0.019 rad·s, and the ability to suppress disturbances below 5 Hz is significantly improved. The system maintains stable control under a +50% large parameter disturbance. This method improves the operational stability of low-speed textile and leather processing tasks, achieving higher fabric quality, reducing material waste, and improving the precision of automated manufacturing.

KEYWORDS

textile machinery, permanent magnet synchronous machine, precision motion control, active disturbance rejection control, robust control

INTRODUCTION

PMSM is widely used in high-performance textile machinery, such as electronic winding frames, digital textile printers, and spinning machines, due to its high efficiency and high power density [1,2]. At low speeds (0-5% of rated speed), the system is susceptible to multi-source uncertainties, including inherent motor characteristics (cogging torque pulsation and flux harmonic distortion) and process-specific disturbances (load variations due to increasing bobbin diameter and mechanical vibrations from looms). These factors

result in increased speed fluctuation, which can directly compromise yarn tension consistency or print image quality, thus reducing overall control accuracy [3,4]. Traditional model-based control methods (such as vector control and sliding mode control) [5,6] rely on precise parameter modeling and are difficult to adapt to complex conditions where parameters are time-varying (such as stator resistance change, moment of inertia drift) and coupled with external disturbances, resulting in insufficient robustness [7-9]. Although traditional ADRC [10] can compensate for disturbances in real-time through an ESO, its fixed gain mechanism has the problem of conflict between observation accuracy and bandwidth in low-speed and high-frequency disturbance scenarios [11], and the control law is limited in its ability to respond to time-varying parameters in real-time [12]. There is an urgent need to improve the algorithm to enhance the robust control performance of PMSMs under low-speed conditions.

This paper focuses on the complex disturbance suppression and parameter uncertainty problems under low-speed working conditions of PMSM. Wu L et al. [13] proposed a compensating fluctuation approximate modeling method to replace finite element analysis for robust design optimization of slot torque, and gave a design scheme with minimal fluctuation impact, but there were still problems in considering the inevitable repeated unit uncertainty and the computational efficiency caused by manufacturing discrete uncertainty. Zuo Y et al. [14] compared the dynamic performance of ADRC system based on ESO and phase-locked loop observer. The experiment verified that the dynamic performance of ADRC system based on ESO was not affected, while ADRC system based on phase-locked loop observer had better suppression ability for low-frequency disturbances. Qu J et al. [15] proposed a new torque pulsation suppression method based on harmonic current control. Through simulation and experimental verification, this method reduced the torque pulsation of PMSM drive in a wide speed range. Wang Y et al. [16] proved through Lyapunov stability analysis that the speed-current single-loop control based on q-axis current constraint constructed by finite time controller could balance PMSM overcurrent protection and dynamic performance. Cao H et al. [17] designed a ROVR controller (reduced-order vector resonant controller) that combined the advantages of complex coefficient filters and vector resonant controllers. Comparisons verified that the proposed ROVR could separate and extract positive-sequence and negative-sequence harmonics while avoiding phase lag and peak points. The spectral coupling characteristics of multi-source disturbances (including low-frequency tooth torque, high-frequency harmonics, and random load disturbances) and the dynamic changes of motor parameters with factors such as temperature and magnetic field saturation

make it difficult for traditional ADRC fixed gain control and single-band disturbance observation methods to meet the needs [18-20].

Zhang Q et al. [21] used fuzzy-ADRC to control the speed of PMSM. Compared with the traditional ADRC system, the system reduced the dynamic response adjustment time from 0.026 s to 0.017 s, but the disturbance range only focused on simulating small disturbances. Tan L N et al. [22] applied a neural network to optimize the observer gain online, but it was difficult to meet the real-time requirements due to the time-consuming training. Tian M et al. [23] developed a non-deterministic periodic frequency band compensation method based on a resonant controller, but its adaptability was limited in other disturbance scenarios. Liu C et al. [24] designed a predictive ESO based on the inherent single sample delay of digital control and the delay of the current measurement low-pass filter to enhance the disturbance estimation accuracy, but there was a control variable jitter problem. Yang Z et al. [25] designed a Kalman anti-disturbance observer based on a Kalman filter, which effectively suppressed the degradation of system performance caused by external disturbances. Its sensitivity to initial values led to unstable convergence speed. Li Z et al. [26] proposed a nonsingular fast terminal sliding mode observer combined with ADRC, which improved robustness but sacrificed control smoothness. The above methods still have significant deficiencies in dynamic observation accuracy, multi-band disturbance decoupling, and online parameter update, and it is difficult to ensure real-time performance.

This paper proposes an improved active disturbance rejection control algorithm that integrates an adaptive extended state observer and fast nonlinear feedback to address the disturbance spectrum mismatch and parameter time-varying issues in PMSM low-speed control. Dynamic bandwidth adjustment of the extended state observer is achieved based on wavelet packet analysis and fuzzy rule base; a three-channel bandpass filter bank (0-50Hz/50-200Hz/200-500Hz) is designed to decouple multi-band interference; hyperbolic tangent function is used to replace the sign function to suppress chattering; recursive least squares method is integrated to identify stator resistance and moment of inertia online and establish time-varying parameter compensation terms.

ALGORITHMS

Adaptive ESO Bandwidth Dynamic Adjustment Method

To address the issue of decreased observation accuracy caused by the mismatch between the fixed bandwidth of the ESO and the spectral characteristics of the disturbance under low-speed operating conditions, a dynamic adjustment method for the ESO bandwidth based on wavelet packet-fuzzy cooperation is proposed. A three-layer wavelet packet decomposition [27,28] algorithm is used to perform online spectral analysis on the residual signal of the PMSM drive system. The 0-500Hz frequency band is divided into 8 sub-bands, and an adaptive threshold method is applied to dynamically track the disturbance spectrum. The order of wavelets and decomposition level are selected to balance time and frequency resolution, ensuring ESO stability without excessive bandwidth or phase lag. The energy proportion of each sub-band is updated every 10ms, and the calculation formula is:

$$E_i = \frac{\sum_{k=1}^{N} |c_{i,k}|^2}{\sum_{i=1}^{8} \sum_{k=1}^{N} |c_{i,k}|^2} \times 100\% \quad (1)$$

In the formula, $c_{i,k}$ is the kth coefficient of the i-th sub-band, and N is the data window length. The main disturbance frequency band is determined by the energy proportion threshold (>15%) derived from wavelet packet statistical characteristics to achieve dynamic tracking of disturbance spectrum features.

A fuzzy mapping rule base for the disturbance energy distribution and the ESO bandwidth is established. The input variables are divided into two types: the main disturbance frequency band energy proportion (Emain): the fuzzy set is defined as {low, medium, high}; the secondary disturbance frequency band energy proportion (Esub): the fuzzy set is defined as {low, medium, high}. The output variable is the bandwidth adjustment factor (β): the fuzzy set is defined as {reduce, maintain, increase}. The Mamdani reasoning [29] method is used to formulate fuzzy rules, and the weighted average method is used to defuzzify to obtain β. The fuzzy reasoning result is updated every 10ms as the basis for adjusting the ESO observation gain. The improved ESO structure diagram is shown in Figure 1.

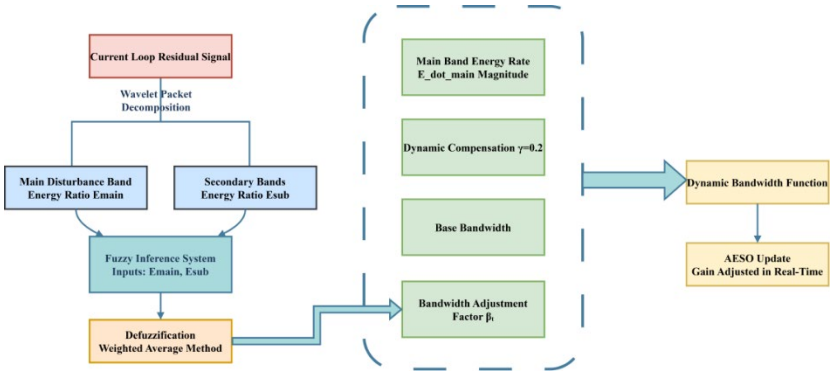

Figure 1. Schematic diagram of the improved ESO structure

The linear observation gain ω_o of the traditional ESO is replaced with a dynamic function:

$$\omega_o(t)=\omega_{o,base}\cdot\beta(t)\cdot(1+\gamma\cdot\frac{|\dot{E}_{main}|}{\max(\dot{E}_{main})}) \quad (2)$$

In the formula, $\omega_{o,base}$ is the reference bandwidth (1000 rad/s); $\beta(t)$ is the fuzzy reasoning result; γ is the dynamic compensation coefficient (taken as 0.2); $\dot{E}_{main}$ is the energy change rate of the main disturbance frequency band.

The adaptive ESO bandwidth dynamic adjustment method is designed to achieve bandwidth adaptation under different disturbance conditions through the corresponding mechanism, and the mechanism is shown in Table 1.

Table 1. Adaptive disturbance mechanism

Operating Condition	Disturbance Characteristics	Detection Criterion	Bandwidth Adjustment Strategy
Steady-State	Stable main disturbance energy	Emain fluctuation <5%/s	Adjust ωo close to base value ωo,base
Disturbance Step	Rapid increase in main disturbance energy	Ėmain > τ (τ = 10%/s)	Increase ωo to 1.2 ×ωo,base for faster response
High-Frequency Noise	Significant increase in high-frequency subband energy	High-frequency band (>400Hz) energy ratio> 8%	Reduce β to 0.8, Reduce ωo to 0.8 × ωo,base to suppress noise amplification

Multi-band Disturbance Decoupling Compensation Strategy

This paper proposes a disturbance decoupling method using a three-channel bandpass filter to address multi-source disturbances like torque pulsation, flux harmonics, and load disturbance under low-speed conditions. A parallel three-channel structure is constructed using a second-order Butterworth filter. The frequency band division is based on the energy distribution characteristics of the PMSM low-speed disturbance. The frequency band division table is shown in Table 2.

Table 2. Frequency band division comparison table

Channel Type	Frequency Range (Hz)	Center Frequency (Hz)	Bandwidth (Hz)	Quality Factor Q	Main Disturbance Sources
Low-frequency Channel	0 - 50	25	50	1.41	Cogging torque ripple (~30Hz fundamental)
Mid-frequency Channel	50 - 200	125	150	1.67	Flux harmonic-induced periodic disturbances
High-frequency Channel	200 - 500	350	300	2	Switching noise and load transient disturbances

Based on Parseval's theorem [30], the Fast Fourier Transform (FFT) is used to calculate the disturbance energy proportion of each channel in real-time. The sliding window FFT (update period 5ms) is performed on the filtered three-channel signal to obtain the frequency domain amplitude $A_i(f)$, and the energy density of each channel is calculated:

$$E_i = \sum_{f=f_{low}}^{f_{high}} |A_i(f)|^2 \ (i=1,2,3) \tag{3}$$

In the formula, E_i represents the total energy density of the i -th channel within the specified frequency range; f_{low} is the lower frequency limit; f_{high} is the upper frequency limit; the subscripts i=1,2,3 correspond to the three signal channels, respectively. After normalization, the weight coefficient is obtained:

$$w_i = \frac{E_i}{\sum_{j=1}^{3} E_j} \tag{4}$$

The weight coefficient is used to dynamically adjust the compensation gain of each channel. For example, when the low-frequency channel energy proportion w_1>60%, the cogging torque compensation mode is started.

To effectively suppress the influence of disturbances in different frequency bands on the PMSM control system under low-speed conditions, this paper designs three types of independent compensation channels: low-frequency channel, medium-frequency channel, and high-frequency channel. Each channel adopts different mathematical models and control strategies to ensure good disturbance suppression performance in its respective frequency band, and improves the stability and robustness of the overall system through a dynamic coordination mechanism.

Low-frequency disturbances mainly come from cogging torque pulsation [31], whose frequency is concentrated around 30 Hz and manifests as periodic interference signals. To this end, this paper constructs a disturbance observer based on a repetitive controller to achieve progressive tracking and compensation of periodic disturbances. For cogging torque pulsation around 30 Hz, a disturbance observer based on a repetitive controller is designed, and its discrete domain form is:

$$U_{rep}(z) = K_r \cdot \frac{z^{-N}}{1-z^{-N}} \cdot E(z) \tag{5}$$

In the formula, $U_{rep}(z)$ is the output of the repetitive controller; K_r is the gain coefficient of the repetitive controller; z^{-N} represents the delay factor; N is the number of sampling points corresponding to the disturbance period; $E(z)$ is the Z-transform form of the tracking error.

Combined with the proportional-integral observation gain L=[kp,ki]T, the disturbance estimate d^ is used for feedforward compensation:u_{comp}=−d^, and the final low-frequency compensation is the superposition of the two:

$$u_{low}=u_{rep}+u_{comp} \tag{6}$$

In the formula, u_{comp} is the feedforward compensation based on the disturbance observation value; d^ is the disturbance value estimated by the ESO.

The medium-frequency disturbance is mainly caused by magnetic flux harmonics [32], which manifests as multiple periodic disturbance components of fixed frequency. To enhance the system's ability to suppress disturbances in this frequency band, this paper adopts a resonant controller for targeted compensation. Considering the single-frequency disturbance dm(t)=Dmsin(ωmt+ϕm), where ωm=2π×125rad/s, the following resonant controller is designed:

$$C_m(s)=\frac{2\zeta\omega_m s}{s^2+2\zeta\omega_m s+\omega_m^2} \tag{7}$$

In the formula, $C_m(s)$ is the transfer function of the resonant controller designed for the medium-frequency band; ζ is the damping coefficient; ω_m is the center angular frequency.

After the controller is discretized and embedded in the dq axis decoupling control loop, the compensation voltage increment is obtained:

$$\begin{aligned}\Delta u_d&=-K_m\cdot Re[C_m(j\omega_m)\cdot I_q]\\ \Delta u_q&=-K_m\cdot Im[C_m(j\omega_m)\cdot I_d]\end{aligned} \tag{8}$$

In the formula, Δu_d and Δu_q are the dq axis voltage compensation increments, respectively; K_m is the medium-frequency compensation gain; I_d and I_q are the current loop feedback values.

The weighting function is applied to limit the gain range:

$$W_m(\omega)=\frac{1}{1+\left(\frac{\omega-\omega_m}{\Delta\omega}\right)^2} \tag{9}$$

The intermediate frequency compensation output is:

$$u_{mid}=W_m(\omega)\cdot(\Delta u_d+\Delta u_q) \tag{10}$$

High-frequency disturbances mainly include PWM (Pulse Width modulation) switching noise and sudden load disturbances [33], which have a wide frequency range and uneven energy distribution. To quickly respond to such disturbances, this paper designs a finite impulse response filter (FIR Filter) as a feedforward compensator and actively suppresses it in combination with the ESO disturbance estimate. Assuming the high-frequency disturbance observation value is $\hat{d}_{hf}$, the designed feedforward compensation term is:

$$u_{hf}=-k_{hf}\cdot\sum_{n=0}^{N-1}h_n\cdot\hat{d}_{hf}(t-nT_s) \tag{11}$$

In the formula, u_{hf} is the high-frequency channel feedforward compensation signal; k_{hf} is the high-frequency gain coefficient; h_n is the FIR filter impulse response coefficient; $\hat{d}_{hf}$ is the high-frequency disturbance observation value; T_s is the system sampling period.

The compensation signal is added to the PWM modulation layer:

$$V'_{PWM}=V_{PWM}+u_{hf} \tag{12}$$

In the formula, V'_{PWM} is the PWM modulation voltage after compensation.

To prevent high-frequency interference from causing oscillation, a low-pass filter is applied to smooth the compensation signal:

$$H_{lp}(s)=\frac{1}{\tau s+1},\tau=\frac{1}{2\pi\times400} \tag{13}$$

In the formula, $H_{lp}(s)$ is the low-pass filter transfer function; τ is the filter time constant. The final output of the high-frequency channel is:

$$u_{high}=H_{lp}(s)\cdot u_{hf} \tag{14}$$

To avoid the risk of dynamic coupling and resonance that may be caused by improper parameter tuning between channels, this paper proposes a dynamic weighted fusion strategy based on the frequency band energy ratio. The strategy calculates the relative proportion of disturbance energy in the corresponding frequency band of each channel in real time, and uses this as a weighting coefficient to perform a weighted summation of the compensation signals of the three channels to generate the final composite compensation amount; the transition band weight function is set in the frequency band overlap area (such as 50Hz, 200Hz):

$$\alpha(f)=\begin{cases}\sin^2\left(\frac{\pi(f-f_c)}{2\Delta f}\right), & f_c-\Delta f\le f\le f_c+\Delta f\\ 0, & \text{otherwise}\end{cases} \tag{15}$$

In the formula, $\alpha(f)$ is the gain soft switching function at the frequency band junction; f_c is the transition band center frequency; Δf is the transition bandwidth. The gain soft switching function $\alpha(f)$ actually defines the effective weight of each compensation channel within its corresponding frequency band. When the operating frequency is within the transition band of adjacent frequency bands, the $\alpha(f)$ values of both channels will be greater than zero simultaneously, indicating that they both participate in the compensation. To ensure the stability of the final synthesized total gain of the compensated signal and prevent overcompensation due to weight superposition, this paper uses normalization processing to generate the final fusion weights. This strategy guarantees that at any frequency point, the sum of the normalized weights of all channels is always equal to 1, thereby achieving smooth, coordinated, and stable compensation for disturbances in different frequency bands.

$$u_{channel}=\begin{cases}u_{channel}, & //E_i//\ge E_{th,i}\\ 0, & \text{otherwise}\end{cases} \tag{16}$$

In the formula, E_i is the disturbance energy of each frequency band; $E_{th,i}$ is the energy suppression threshold of the corresponding frequency band.

Design of Fast Nonlinear Feedback Control Law

This paper proposes a composite control law based on the hyperbolic tangent function to solve high-frequency chattering and improve dynamic response using an adaptive gain mechanism [34]. The hyperbolic tangent function tanh(·) is used to replace the sign function sign(·) in the traditional sliding mode control law to construct a continuous control law to suppress chattering. The sliding surface is defined as $s=c_1e+c_2\dot{e}$, where e is the tracking error. c1 and c2 are the sliding mode coefficients, and the improved control law form is:

$$u_{tanh}=-k\cdot\tanh\left(\frac{s}{\varepsilon}\right) \quad (17)$$

In the formula, ε=0.1 is the boundary layer thickness, and k is the control gain (initial value k=15). This design smoothly transitions to linear control when |s|<ε near the sliding surface to avoid high-frequency switching. The control law structure comparison diagram is shown in Figure 2.

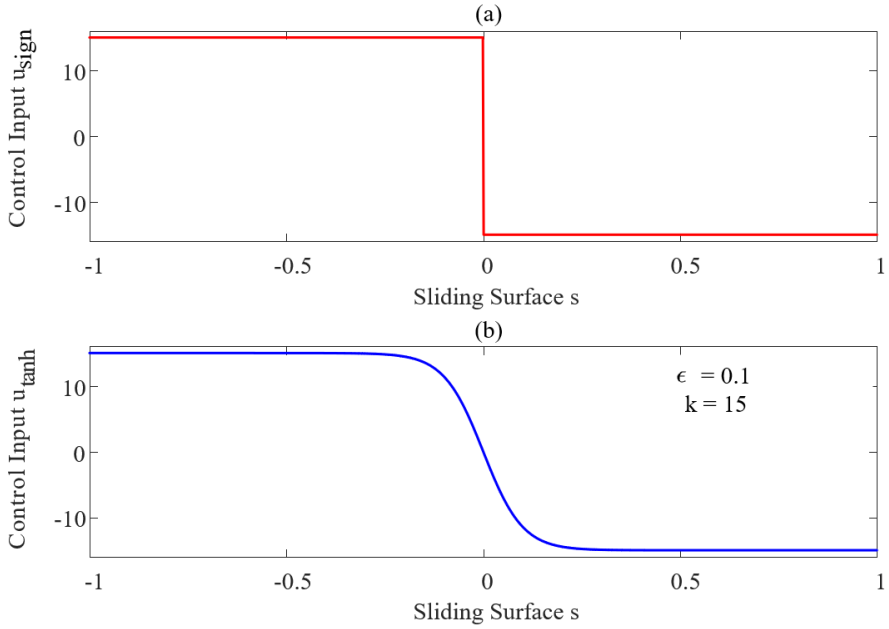

Figure 2. Control law structure comparison: (a) Traditional sign function control law; (b) Improved hyperbolic tangent control law

To improve the system's convergence speed, the exponential approach law $\dot{s}=-q\cdot sign(s)-ps$ is coupled with the sliding surface design for optimization. The generalized disturbance estimate d^ provided by the adaptive ESO is defined, and then the improved control law is:

$$u=u_0+u_{tanh}-\hat{d} \tag{18}$$

In the formula, u_0 is the feedforward control term, and u_{tanh} is the parameter. Then, q and p are dynamically adjusted:

$$\begin{aligned} q&=q_0+\alpha\cdot\|\dot{s}\,/\!/ \\ p&=p_0+\beta\cdot\|s\,/\!/ \end{aligned} \tag{19}$$

In the formula, q_0=8 and p_0=5 are the basic values, and α=0.3 and β=0.2 are the adaptive coefficients. To ensure the stability of the proposed improved ADRC closed-loop system, this paper analyzes the convergence of the complete system, including the dynamic characteristics of the controller and observer.

Establish a closed-loop error system model, defining the tracking error $e$and the extended state estimation error vector $\mathbf{e}_0$. The system dynamics are given by $\ddot{e}=-\alpha_1 e-\alpha_2\dot{e}+\mathbf{c}^T\mathbf{e}_0$, where $\mathbf{c}$is a constant vector. Construct a Lyapunov function $V=\frac{1}{2}e^2+\frac{1}{2}(\dot{e})^2+\frac{1}{2}k\cdot\|\mathbf{e}_0\|^2$. Taking the time derivative of Vyields $\dot{V}=e\dot{e}+\dot{e}\ddot{e}+k\mathbf{e}_0^T\dot{\mathbf{e}}_0$. Substituting the system dynamics, we obtain $\dot{V}=e\dot{e}+\dot{e}(-\alpha_1 e-\alpha_2\dot{e}+\mathbf{c}^T\mathbf{e}_0)+k\mathbf{e}_0^T\dot{\mathbf{e}}_0$. By designing controller parameters $\alpha_1$and $\alpha_2$such that α_2>0and applying Young's inequality to handle cross terms, it follows that $\dot{V}\le-\alpha V+\beta$, where α>0and $\beta\ge$0are constants. This demonstrates that the tracking error and observer error are ultimately bounded under bounded disturbances.

Let e represent the tracking error and e_0 represent the Euclidean norm of the extended state estimation error vector $\|e_{0,vec}\|=\sqrt{\sum_{i=1}^{n}e_{0,i}^2}$ where n is the dimension of the ESO state vector, and construct a Lyapunov function containing two error components:

$$V=\frac{1}{2}e^2+\frac{1}{2}(\dot{e})^2+\frac{1}{2}k\cdot e_0^2 \tag{20}$$

$k>0$ is a positive constant. Let $e$represent the tracking error and $e_0$represent the Euclidean norm of the extended state estimation error vector $\|e_{0,vec}\|=\sqrt{\sum_{i=1}^{n} e_{0,i}^2}$where $n$is the dimension of the ESO state vector. Construct a quadratic Lyapunov function $V=\frac{1}{2}e^2+\frac{1}{2}(\dot{e})^2+\frac{1}{2}k\cdot e_0^2$where $k>0$is a positive constant. Taking the time derivative of Vyields $\dot{V}=e\dot{e}+\dot{e}\ddot{e}+ke_0\dot{e}_0$. Substituting the system dynamics $\ddot{e}=-\alpha_1 e-\alpha_2\dot{e}+c^T e_0$where $c$is a constant vector, it follows that $\dot{V}\leq-\alpha V+\beta$, where $\alpha>0$and $\beta\geq0$are constants determined by the observer bandwidth $\omega_o$and controller parameters $q$and p. The sufficient conditions for stability require $\omega_o>300$rad/s and $q>6$to ensure $\alpha>0$, which guarantees the ultimate boundedness of both tracking error and observer error under bounded disturbances.

Parameter Time-Varying Compensation Mechanism

This paper designs an online parameter identification module based on RLS to handle time-varying characteristics of stator resistance Rs and moment of inertia J, and establishes a dynamic parameter compensation mechanism.

(1) RLS online identification module

The improved RLS method is used to construct the parameter online identification model. The dq axis voltage formula is used as the identification basis:

$$\begin{cases} u_d=R_s i_d-\omega L_q i_q+\dot{\psi}_d \\ u_q=R_s i_q+\omega L_d i_d+\dot{\psi}_q \end{cases} \tag{21}$$

In the formula, u_d is the direct axis voltage sampling value; R_s is the stator resistance; i_d is the direct axis current; ω is the rotor angular velocity; L_q is the quadrature axis inductance; i_q is the quadrature axis current; $\dot{\psi}_d$ is the direct axis flux change rate; u_q is the quadrature axis voltage sampling value; L_d is the direct axis inductance; $\dot{\psi}_q$ is the quadrature axis flux change rate. The formula is simplified into a linear regression form:

$$y(k)=\phi^T(k)\theta(k)+v(k) \tag{22}$$

In the formula, y(k) is the observation vector; ϕ(k) is the regression matrix; θ(k) is the parameter vector to be identified; v(k) is the system noise.

RLS parameter estimation is updated every 5ms, with a data window length of 200 points. During the interval between updates, the system uses a zero-order hold to provide the previously identified parameter values as constants to the feedforward compensation stage. ESO continues to run during this period, estimating and compensating for the total disturbance, including unmodeled dynamics, external disturbances, and parameter prediction errors. After the new parameter estimation is updated, the feedforward compensation term immediately switches to the new value, achieving periodic correction of time-varying parameters. The RLS recursive process is shown in Figure 3:

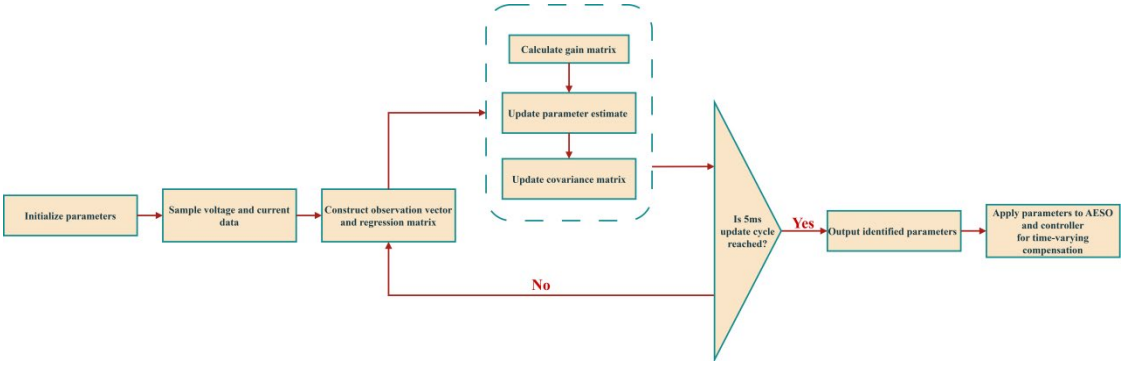

Figure 3. RLS recursive process

(2) Design of parameter change rate warning threshold

To quantify the impact of parameter time variation on system stability, the parameter change rate index is defined:

$$\eta(k)=\frac{//\hat{\theta}(k)-\hat{\theta}(k-1)//}{//\hat{\theta}(k-1)//}\times 100\% \tag{23}$$

In the formula, $\hat{\theta}(k)$ is the parameter estimate. The root mean square error is calculated through the sliding window:

$$\varepsilon_{rms}=\sqrt{\frac{1}{N}\sum_{i=1}^{N}(\eta(i)-\overline{\eta})^2} \tag{24}$$

In the formula, $\bar{\eta}$ is the mean value of the parameter change rate; To establish an objective basis for triggering the update mechanism, the warning threshold εth is derived from statistical analysis of system noise. Specifically, during a stable initial period, the standard deviation (σ_η) of the parameter change rate is calculated. The dynamic warning threshold is then set as $\varepsilon_{th} = k * \sigma_\eta$, where k is a safety factor . When $\varepsilon_{rms} > \varepsilon_{th}$, the parameter update check mechanism is triggered.

(3) Parameter update trigger and compensation injection

The activation of the full parameter update mechanism requires confirmation beyond the initial warning. A secondary criterion is employed: when the parameter change rate $\eta(k)>k_2\times\sigma_\eta$ and this condition persists for more than N consecutive sampling cycles, the RLS parameter update mechanism is activated. The compensation strategy is divided into the following steps:

(1) the parameter deviation is calculated:

$$\begin{aligned}\Delta R_s&=\hat{R}_s(k)-R_s^{nom}\\ \Delta J&=\hat{J}(k)-J^{nom}\end{aligned} \tag{25}$$

In the formula, R_s^{nom} is the nominal value of the stator resistance; ΔJ is the moment of inertia deviation; J^{nom} is the nominal value of the moment of inertia;

(2) Compensation terms are generated:

$$\begin{aligned}\Delta u_d&=-\frac{\Delta R_s}{R_s^{nom}}u_d^{nom}\\ \Delta u_q&=-\frac{\Delta J}{J^{nom}}u_q^{nom}\end{aligned} \tag{26}$$

In the formula, u_d^{nom} is the nominal value of the direct-axis voltage; u_q^{nom} is the nominal value of the quadrature-axis voltage;

(3) The compensation amount is added to the voltage command:

$$\begin{aligned}u_d^{'}&=u_d+\Delta u_d\\ u_q^{'}&=u_q+\Delta u_q\end{aligned} \tag{27}$$

EXPERIMENTAL VERIFICATION

Experimental Design

To verify the control performance of the improved ADRC under low-speed conditions, a MATLAB-based digital simulation is used with a high-fidelity PMSM model, including characteristics such as cogging torque harmonics, flux distortion, and nonlinear friction. The experimental condition is set to 2% of the rated speed (30rpm). Under this condition, the cogging torque pulsation frequency is about 12Hz; the flux harmonic distortion is significant; the load disturbance has a significant impact on speed stability. The improved ADRC controller is compared with the traditional ADRC, PID (Proportion Integral Differential) algorithm, and sliding mode control algorithm. All control strategies are operated under the same initial conditions to ensure the effectiveness of the comparison. The comparison algorithm parameter settings are shown in Table 3. To verify the effectiveness of the proposed control strategy, the controlled motor (PMSM) was a 3kW surface-mount permanent magnet synchronous motor. The motor's pole-slot matching design is 12 slots and 8 poles, which helps reduce cogging torque. The inverter used was an Infineon FS800R07A1E3B11 module, forming a three-phase full-bridge circuit. The motor phase current was sampled using a LEM Hall current sensor.

Table 3. Comparison algorithm parameter settings

Control Strategy	Parameter Name	Value	Description
Traditional ADRC	Observer Bandwidth ω_o	1000 rad/s	ESO bandwidth
	Controller Bandwidth ω_c	150 rad/s	Nonlinear feedback controller bandwidth
Proposed ADRC	Adaptive ESO Initial Bandwidth $\omega_{o,0}$	800 rad/s	Base bandwidth with dynamic range (800–1200 rad/s)
	Fuzzy Rule Base Energy Threshold Eth	Low-frequency: 15%, Mid-frequency: 10%, High-frequency: 5%	Disturbance energy distribution and bandwidth matching rules
	RLS Forgetting Factor	0.98	Dynamic weighting for online pa-

			rameter identification
	Multi-band Compensation Gains klow,mid,high	Low-frequency: 1.2, Mid-frequency: 1.0, High-frequency: 0.8	Disturbance suppression weights for different frequency bands
PID Control	Proportional Gain Kp	0.8	Optimized via Ziegler-Nichols criterion
	Integral Time Constant Ti	0.05 s	
Sliding Mode Control	Sliding Mode Gain k	12	Switching function gain
	Reaching Law Coefficient	0.5	Exponential reaching law parameter

Low-speed Tracking Accuracy Evaluation

The integral absolute error (IAE) index is used to evaluate speed response data under a 0.5Hz sinusoidal command, with speed response curves collected using a high-precision photoelectric encoder.

$$IAE=\int_0^T |\omega_d(t)-\omega(t)|dt \quad (28)$$

In the formula, $\omega_d(t)$ is the command speed; $\omega(t)$ is the actual speed output; the integral period T=2s covers the complete period of the sinusoidal command. All control strategies repeat the experiment 5 times under the same initial conditions, take the average value as the final result, and mark the maximum and minimum values as the error band. The speed tracking curve comparison in Figure 4 shows that the improved ADRC has minimal fluctuation and a maximum error of 0.05 rad/s, while the other methods show larger errors and fluctuations. The experimental data in Figure 5(a) shows that the IAE value of the improved ADRC is 0.019 rad·s, significantly lower than the 0.028 rad·s of traditional ADRC, 0.041 rad·s of PID, and 0.036 rad·s of sliding mode control.

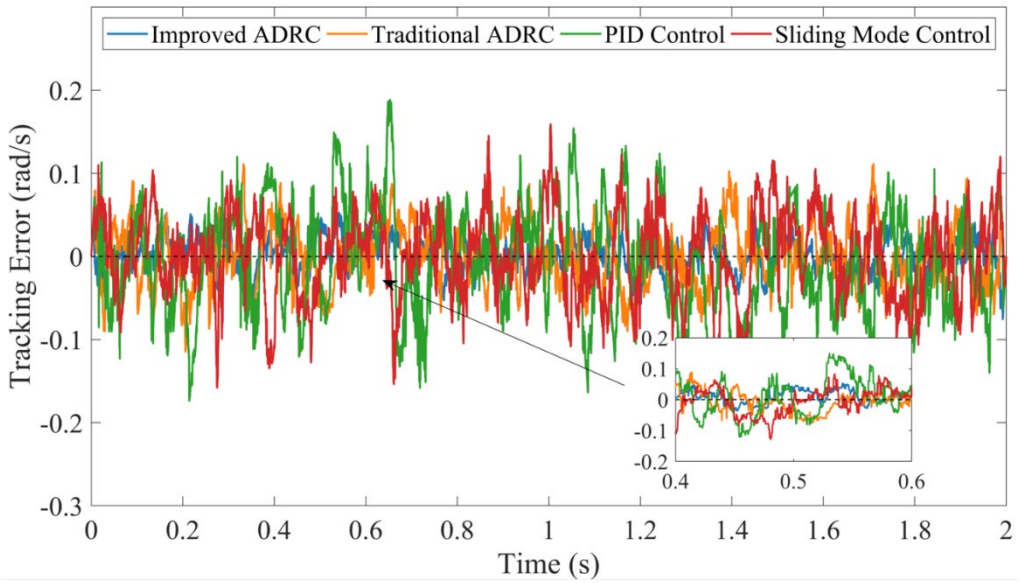

Figure 4. Comparison of speed tracking curves

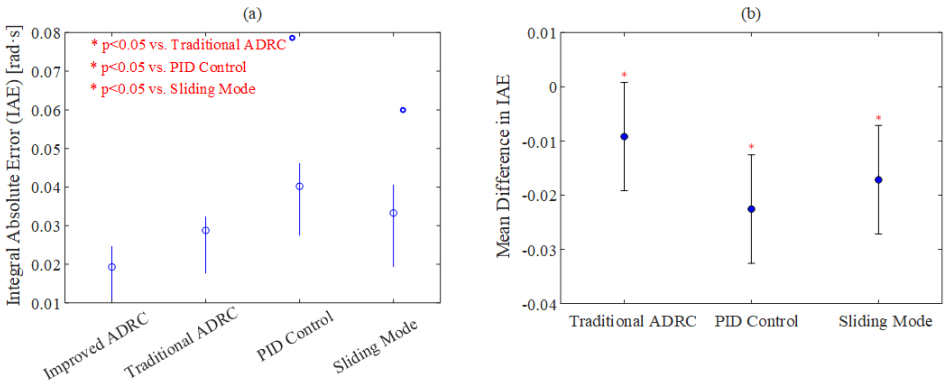

Figure 5. Comparison of IAE data distribution under different control methods

To clarify the specific differences between the improved ADRC and the comparison algorithm, the Tukey post hoc test (Tukey-Kramer method) is further performed to calculate the confidence interval of the mean difference of each group. The results are shown in Figure 5 (b). The mean difference of IAE between the improved ADRC and the traditional ADRC is -0.009 rad·s; the mean difference with PID control is -0.022 rad·s; the mean difference with sliding mode control is -0.017 rad·s. The improved method is superior to all the compared algorithms in low-speed tracking accuracy. This result verifies the stability of the improved method in suppressing cogging torque pulsation and parameter time-varying disturbance.

Multi-frequency Disturbance Suppression Capability

A multi-band composite disturbance signal with 5Hz, 20Hz, and 100Hz components is applied to the motor control system, and disturbance response characteristics are quantified by q-axis current harmonic analysis. The disturbance is superimposed on the d-axis voltage command under low-speed conditions (30rpm). The current waveform during the disturbance loading period is recorded through a high-speed data acquisition system (sampling rate 20kHz), and the fast Fourier transform is used to extract the current harmonic content of each frequency band. The torque pulsation coefficient TR is then calculated to quantitatively evaluate the suppression effect of different control methods on multi-frequency disturbances.

The torque torsion coefficients under different algorithm control are shown in Table 4. The average electromagnetic torque of the improved ADRC is 1.23 N·m, ensuring stable output. ΔT is only 0.010 N·m, and the corresponding torque pulsation coefficient TR is 0.82%, which is significantly better than traditional ADRC (TR=2.15%), PID control (TR=3.76%), and sliding mode control (TR=2.94%). The ΔT of the traditional ADRC is 2.6 times that of the improved method, while the PID and sliding mode control reach 0.045 N·m and 0.035 N·m, respectively, indicating that its ability to suppress complex disturbances is weak, and the system stability and low-speed operation smoothness are significantly affected. The improved ADRC can show better anti-disturbance performance under multi-frequency disturbances.

Table 4. Comparison of torque disturbance characteristics under different control algorithms

Control Strategy	Average Electromagnetic Torque T_avg (N·m)	Torque Fluctuation Amplitude ΔT (N·m)	Torque Ripple TR (%)
Improved ADRC	1.23	0.01	0.82
Traditional ADRC	1.21	0.026	2.15
PID Control	1.19	0.045	3.76
Sliding Mode	1.2	0.035	2.94

To further compare the disturbance response differences between the improved ADRC and traditional ADRC, PID, and sliding mode control in the frequency domain, the power spectrum (PS) of the q-axis current is analyzed to identify the distribution characteristics of the disturbance energy in the frequency do-

main. Figure 6 shows the frequency domain response characteristics of the q-axis current under different control strategies under multi-frequency disturbance loading conditions. The horizontal axis is the frequency (Hz), ranging from 0 to 200Hz, and the vertical axis is the PS (unit: dB) of the current signal, which is used to reflect the distribution of disturbance energy in each frequency band. The disturbance response of the improved ADRC in the low-frequency band below 5Hz is significantly lower than that of the traditional ADRC, PID control, and sliding mode control, and its maximum spectrum amplitude is only -90dB. At the same frequency point, the traditional ADRC, PID, and sliding mode control achieve -40dB, -35dB, and -38dB, respectively. This indicates that these three methods have limited suppression capability under low-frequency disturbances, resulting in significant residual disturbance energy in the system. In contrast, the proposed improved ADRC method achieves a superior suppression of -90dB, demonstrating its significantly enhanced performance in mitigating low-frequency interference. The improved ADRC effectively matches the disturbance spectrum characteristics through the bandwidth dynamic adjustment mechanism of the AESO, so that the disturbance energy is greatly attenuated. The disturbance suppression capability is significantly improved compared with the traditional ADRC, and no additional phase lag or steady-state error is applied, maintaining good dynamic response performance.

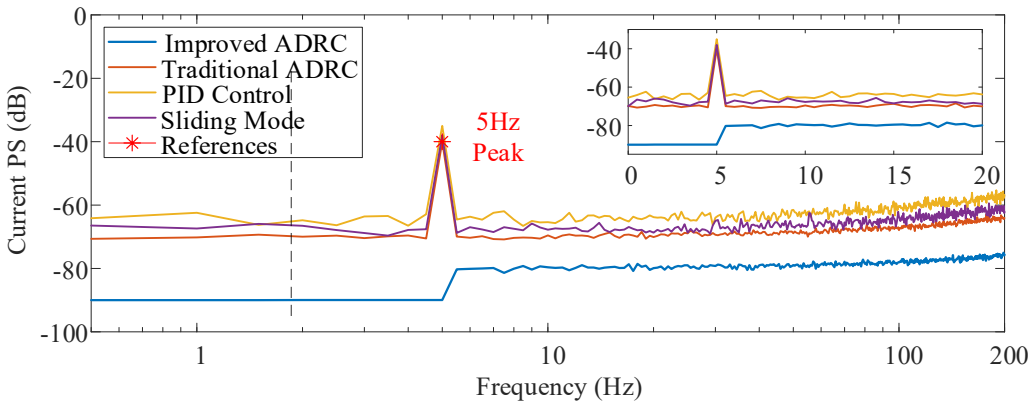

Figure 6. Frequency domain disturbance response spectrum

The experimental results show that the improved ADRC adopts an effective combination of adaptive ESO structure and multi-band disturbance decoupling compensation mechanism, and exhibits excellent disturbance suppression capability in the frequency band below 5Hz. The adaptive ESO extracts the disturbance spectrum characteristics in real-time through wavelet packet analysis and dynamically adjusts the ob-

server bandwidth according to the disturbance energy distribution, so that it can precisely track key disturbance components such as 5Hz, 20Hz, and 100Hz, thereby realizing precise estimation and compensation of tooth slot torque pulsation, flux harmonics, and load disturbances. The traditional ADRC uses a fixed bandwidth setting, which makes it difficult to accurately match the disturbance characteristics when facing complex disturbance spectra, resulting in increased observation errors; PID and sliding mode control lack a feedforward disturbance compensation mechanism and rely only on feedback regulation, which results in delayed response and easy to cause high-frequency jitter, ultimately manifesting as a larger spectrum peak and lower anti-disturbance performance. The improved ADRC achieves effective suppression of multi-source composite disturbances without sacrificing system stability, significantly improving the robustness and operating stability of PMSMs under low-speed conditions.

In summary, the multi-frequency disturbance scenario is constructed by the voltage injection method, and the suppression capability of the improved ADRC algorithm for multi-band disturbances is systematically evaluated by combining the q-axis current harmonic analysis and spectrum decomposition technology. The experimental results show that the proposed adaptive bandwidth adjustment and multi-band decoupling compensation mechanism can effectively identify and suppress disturbances in different frequency bands, thereby significantly improving the anti-disturbance performance and control stability of the PMSM under low-speed conditions.

Parameter Robustness Verification

The load inertia mutation test is conducted under low-speed conditions (30rpm) with ±50% and -30% inertia disturbances applied. The controller uses RLS to identify changes in stator resistance and inertia parameters, with a parameter update mechanism triggered when the change rate exceeds 3%/s.

The parameter mutation response curve in Figure 7 shows the speed tracking error response curve of the PMSM under different control strategies under the condition of ± parameter perturbation (+50% and -30%) of the load inertia. The horizontal axis is time (seconds), and the vertical axis is the speed tracking error (rad/s), which reflects the controller's tracking accuracy of the command speed. It can be seen that after applying a +50% moment of inertia disturbance at 1s, the error of the improved ADRC rises rapidly to about 0.16rad/s and converges quickly, while the errors of the traditional ADRC, PID control, and sliding mode control reach 0.29rad/s, 0.48rad/s, and 0.40rad/s, respectively, and show more obvious fluctuations and a longer recovery process. Then, when it switches to -30% inertia disturbance at 1.5s, the improved ADRC can

still maintain a small error and complete dynamic adjustment in a short time, showing stronger anti-disturbance ability and robustness.

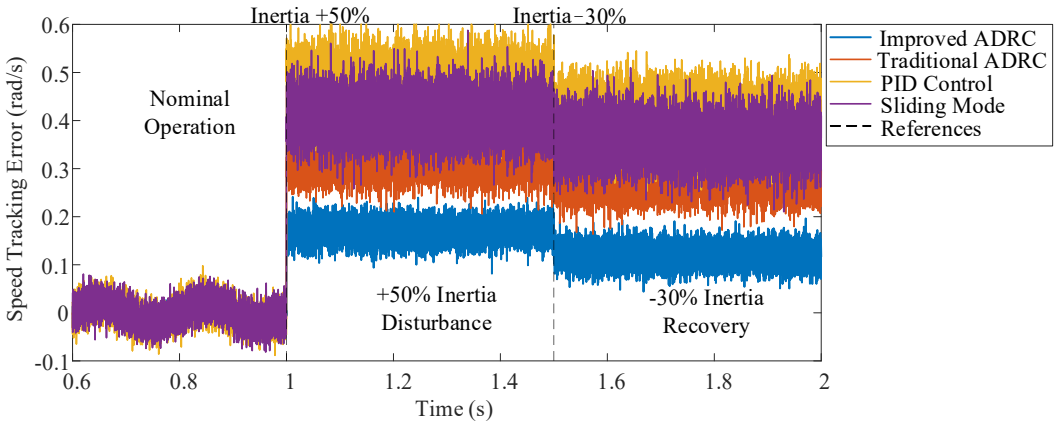

Figure 7. Parameter mutation response curve

The experiment further uses the Pearson correlation coefficient R to perform statistical analysis on the parameter change rate and its corresponding tracking error peak. In multiple repeated experiments, the parameter change rate corresponding to each disturbance event and its corresponding tracking error peak are recorded, and their linear correlation is calculated. Table 5 shows the statistical relationship between the parameter change rate and the speed tracking error peak under different control strategies in the parameter mutation experiment. From the data, it can be seen that when the parameter change rate of the improved ADRC reaches 5.6%/s, its maximum speed error is still maintained within 0.20 rad/s, while the traditional ADRC, PID, and sliding mode control errors reach 0.43 rad/s, 0.53 rad/s, and 0.47 rad/s, respectively, which is significantly better than the other three comparison methods. The Pearson correlation coefficient of the improved ADRC is only 0.23, indicating that there is basically no obvious linear dependence between its error change and parameter perturbation, showing good adaptive ability.

Table 5. Correlation analysis between parameter change rate and speed tracking error peak

Control Strategy	Parameter Variation Rate (%/s)	Peak Tracking Error (rad/s)	Pearson Correlation Coefficient R
Improved ADRC	0.6	0.12	0.23
	1.1	0.14	
	2.0	0.15	
	3.2	0.17	
	4.8	0.19	
	5.6	0.20	
Traditional ADRC	0.7	0.23	0.68
	1.3	0.27	
	2.2	0.31	
	3.5	0.36	
	4.9	0.40	
	5.8	0.43	
PID Control	0.5	0.32	0.79
	1.2	0.36	
	2.3	0.41	
	3.4	0.46	
	4.7	0.50	
	5.9	0.53	
Sliding Mode	0.8	0.27	0.72
	1.4	0.30	
	2.5	0.35	
	3.6	0.39	
	4.8	0.43	
	6.0	0.47	

Dynamic Response Performance

A step command is applied to the control system under low-speed conditions (30rpm), and the speed response curve is recorded. The rise time Tr is defined as the time for the speed to rise from 10% to 90% of the target value. All tests are repeated 5 times under the same initial conditions. The average value is taken as the final evaluation index, and the standard deviation is calculated to reflect the degree of data dispersion.

Figure 8 shows the speed response curve of each method under the same step input. The rise time Tr=0.23s of the improved ADRC under the step command (0→30rpm) is significantly better than the 0.35s of the traditional ADRC, the 0.48s of the PID control, and the 0.41s of the sliding mode control, indicating that it has faster response speed and stronger dynamic adjustment ability. The analysis results show that the advantages of improved ADRC in dynamic response mainly come from the hyperbolic tangent nonlinear feedback control law and adaptive gain adjustment mechanism it applies. By replacing the traditional sign function with a smooth and continuous hyperbolic tangent function, the discontinuity problem of the control signal is effectively alleviated, and the uncertainty caused by high-frequency jitter is reduced. The design structure combining the exponential approach law with the sliding surface enhances the speed and stability of the system state convergence to the sliding surface, enabling the system to quickly adjust the control input when facing step excitation and shorten the response delay. The gain adaptive adjustment module dynamically adjusts the feedback strength according to the error amplitude, while improving the response speed and avoiding excessive control action that causes system instability or excessive overshoot.

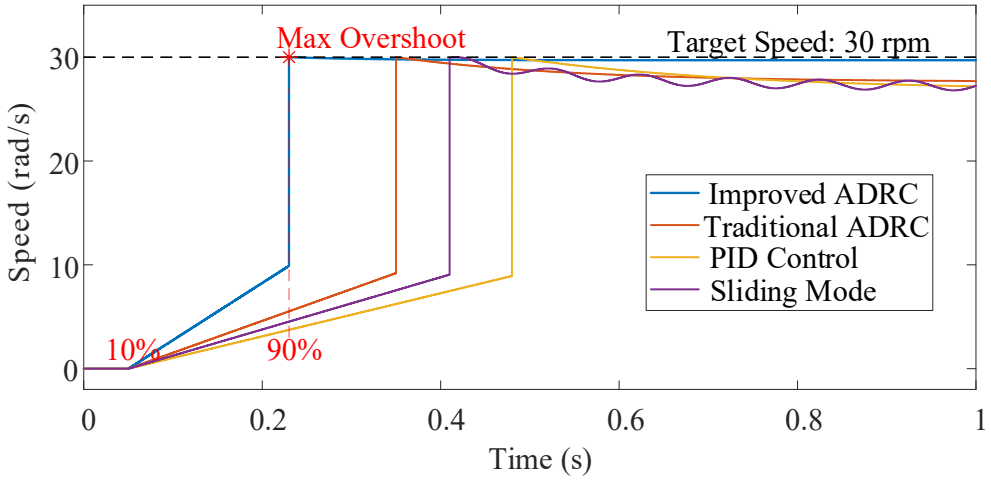

Figure 8. Dynamic response comparison

CONCLUSIONS

This paper proposes an improved ADRC algorithm to address the problem of poor control accuracy and disturbance susceptibility of PMSMs drives within high-precision textile machinery under low-speed conditions. The maximum spectrum amplitude of the improved method is only -90dB under the disturbance of the frequency band below 5Hz; under the condition of +50% parameter perturbation, the speed fluctuation standard deviation rises rapidly to 0.16rad/s and converges quickly; the dynamic response rise time Tr=0.23s, which is better than the traditional ADRC (Tr=0.35s) and other comparison strategies. This study still has certain limitations. Further exploration could involve applying this method to real-time yarn tension control in advanced winding systems or multi-axis synchronization in complex digital knitting machines, addressing multi-physics coupling control scenarios in the textile industry.

Author Contributions

Conceptualization-Xiaoyan Han; methodology-Xiaoyan Han; formal analysis-Xiaoyan Han; investigation-Xiaoyan Han; resources-Xiaoyan Han; writing-Xiaoyan Han. The author has read and agreed to the published version of the manuscript.

Conflicts of Interest

The author declares no conflict of interest.

Funding

This research was funded by Name of "Research and Application of Key Technologies for Intelligent Control System of Fire Inspection Robot", grant number 25A470014.

Acknowledgements

Not applicable.

REFERENCES

[1] Djiev SN, Pavlov LI. Computer-Aided Design, Engineering, and Manufacturing. Boca Raton, Florida, USA: CRC Press; 2019; Automated Systems Techniques for On-Line Quality and Production Control in the Manufacture of Textiles. p. 1-8. doi: 10.1201/9780429124303-8

[2] Xiao Y, Zhang Z, Liu Z, Liu W, Gao N, Zhou W, et al. Optimal analysis and application of the warp tension control system for a rapier loom. Textile Research Journal. 2022; 92(7-8):1213-1225. doi: 10.1177/00405175211053662

[3] Zhang H, Xia H, Lu Y, Wu J, Zhang X, Wei Y. Tension control of a yarn winding system based on the nonlinear active disturbance-rejection control algorithm. Textile Research Journal. 2022; 92(23-24):5049-5065. doi: 10.1177/00405175221114658

[4] Ma S, Zong X, Li S. Textile winding tension control based on Active Disturbance Rejection Control. 2022 IEEE 6th Information Technology and Mechatronics Engineering Conference (ITOEC). 04-06 March 2022; Chongqing, CN. New York, NY, USA: IEEE; 2022. p. 42-46. doi: 10.1109/itoec53115.2022.9734316

[5] Silber S, Sloupensky J, Dirnberger P, Moravec M, Amrhein W, Reisinger M. High-speed drive for textile rotor spinning applications. IEEE Transactions on Industrial Electronics. 2013; 61(6):2990-2997. doi: 10.1109/TIE.2013.2258308

[6] Zhang Y, Meng Z, Sun Z, Li C. Control strategy for single-layer warp tension in a carbon fiber 3D loom based on fixed-time theory and sliding mode theory. Textile Research Journal. 2025; 95(9-10):1108-1124. doi: 10.1177/00405175241286541

[7] Ziane D, Zeghlache S, Benkhoris MF, Djerioui A. Robust Control Based on Adaptative Fuzzy Control of Double-Star Permanent Synchronous Motor Supplied by PWM Inverters for Electric Propulsion of Ships. Mathematics. 2024; 12(10):1451. doi: 10.3390/math12101451

[8] Kumar LA. Automation in textile machinery: Instrumentation and control system design principles. Boca Raton, Florida, USA: CRC Press; 2018. Available from: http://localhost/handle/Hannan/3496

[9] Xie F, Hong W, Qiu C. Speed fluctuation suppression of PMSM using active disturbance rejection and feedback compensation control. IET Electric Power Applications. 2021; 15(8):1056-1067. doi: 10.1049/elp2.12079

[10] Hezzi A, Ben Elghali S, Bensalem Y, Zhou Z, Benbouzid M, Abdelkrim MN. ADRC-based robust and resilient control of a 5-phase PMSM driven electric vehicle. Machines. 2020; 8(2):17. doi: 10.3390/machines8020017

[11] Tian M, Wang B, Yu Y, Dong Q, Xu D. Enhanced One Degree-of-Freedom ADRC with Sampled-Data Iterative Learning Controller for PMSM Uncertain Speed Fluctuations Suppression. IEEE Transactions on Transportation Electrification. 2024; 10(4):8321-8335. doi: 10.1109/TTE.2024.3351097

[12] Luo J, Wang L, Liu B. Low-speed control of PMSM based on ADRC+ FOPID. Systems Science & Control Engineering. 2021; 9(1):73-87. doi: 10.1080/21642583.2020.1863279

[13] Wu L, Chen H, Yu T, Sun C, Wang L, Ye X, et al. Robust design optimization of the cogging torque for a PMSM based on manufacturing uncertainties analysis and approximate modeling. Energies. 2023; 16(2):663. doi: 10.3390/en16020663

[14] Zuo Y, Mei J, Jiang C, Yuan X, Xie S, Lee CHT. Linear Active Disturbance Rejection Controllers for PMSM Speed Regulation System Considering the Speed Filter. IEEE Transactions on Power Electronics. 2021; 36(12):14579-14592. doi: 10.1109/TPEL.2021.3098723

[15] Qu J, Jatskevich J, Zhang C, Zhang S. Torque ripple reduction method for permanent magnet synchronous machine drives with novel harmonic current control. IEEE Transactions on Energy Conversion. 2021; 36(3):2502-2513. doi: 10.1109/TEC.2021.3056557

[16] Wang Y, Yu H, Liu Y. Speed-current single-loop control with overcurrent protection for PMSM based on time-varying nonlinear disturbance observer. IEEE Transactions on Industrial Electronics. 2021; 69(1):179-189. doi: 10.1109/TIE.2021.3051594

[17] Cao H, Deng Y, Li H, Wang J, Liu X, Sun Z, et al. Generalized active disturbance rejection with reduced-order vector resonant control for PMSM current disturbances suppression. IEEE Transactions on Power Electronics. 2023; 38(5):6407-6421. doi: 10.1109/TPEL.2023.3237331

[18] Wang Y, Yu HT, Feng NJ, Wang YC. Non-cascade backstepping sliding mode control with three-order extended state observer for PMSM drive. IET Power Electronics. 2020; 13(2):307-316. doi: 10.1049/iet-pel.2019.0819

[19] Cao Z, Mao J, Dong X, Madonski R, Zhang C, Yang J. Composite generalized dynamic predictive control with self-tuning horizon for wide-range speed regulation of PMSM drives. IEEE Transactions on Energy Conversion. 2023; 39(1):659-674. doi: 10.1109/TEC.2023.3329931

[20] Cui X, Xu P, Gu H, Wang L, Xiong X, Tan H. The primary frequency modulation control strategy based on fuzzy active disturbance rejection control for gas turbines. Measurement and Control. 2025; 58(1):15-23. doi: 10.1177/0020294024124765

[21] Zhang Q, Zhang C. Speed Control of PMSM Based on Fuzzy Active Disturbance Rejection Control under Small Disturbances. Applied Sciences. 2023; 13(19):10775. doi: 10.3390/app131910775

[22] Tan LN, Cong TP, Cong DP. Neural network observers and sensorless robust optimal control for partially unknown PMSM with disturbances and saturating voltages. IEEE Transactions on Power Electronics. 2021; 36(10):12045-12056. doi: 10.1109/TPEL.2021.3071465

[23] Tian M, Wang B, Yu Y, Dong Q, Xu D. Robust adaptive resonant controller for PMSM speed regulation considering uncertain periodic and aperiodic disturbances. IEEE Transactions on Industrial Electronics. 2022; 70(4):3362-3372. doi: 10.1109/TIE.2022.3177759

[24] Liu C, Zhao Z, You Y, Duan X, Chen L, Xiao X. Active disturbance rejection current controller with time delay compensation predictive ESO for aircraft PMSM drive. IET Electric Power Applications. 2025; 19(1):e12522. doi: 10.1049/elp2.12522

[25] Yang Z, Miao C, Sun X, Guo D. Robust model predictive torque control of interior pmsm drives with kalman-based disturbance observer. IEEE Transactions on Transportation Electrification. 2023; 10(2):2434-2444. doi: 10.1109/TTE.2023.3296684

[26] Li Z, Zhang Z, Wang J, Wang S, Chen X, Sun H. ADRC control system of PMLSM based on novel non-singular terminal sliding mode observer. Energies. 2022; 15(10):3720. doi: 10.3390/en15103720

[27] Xia Y, Li X, Luo Y. Inter-turn short circuit fault detection of PMSM based on wavelet packet energy spectrum and CEEMDAN-HT. Journal of Electrical Engineering & Technology. 2024; 19(3):1379-1393. doi: 10.1007/s42835-023-01597-7

[28] Ye M, Gong R, Wu W, Peng Z, Jia K. Fault Diagnosis of Permanent Magnet Synchronous Motor Based on Wavelet Packet Transform and Genetic Algorithm-Optimized Back Propagation Neural Network. World Electric Vehicle Journal. 2025; 16(4):238. doi: 10.3390/wevj16040238

[29] Khanh PQ, Anh HPH. Novel sensorless PMSM speed control using advanced fuzzy MRAS algorithm. Arabian Journal for Science and Engineering. 2022; 47(11):14531-14542. doi: 10.1007/s13369-022-06834-1

[30] Deng W, Huang J, Qian Z, Qian C, Zhong D. A random pulse position-based selective noise cancellation modulation method for SVPWM driven PMSMs. IEEE Transactions on Energy Conversion. 2022; 37(3):2190-2198. doi: 10.1109/TEC.2022.3160462

[31] Bu F, Yang Z, Gao Y, et al. Speed ripple reduction of direct-drive PMSM servo system at low-speed operation using virtual cogging torque control method. IEEE Transactions on Industrial Electronics. 2020; 68(1):160-174. doi: 10.1109/TIE.2019.2962400

[32] Hou Q, Zuo Y, Sun J, Pan Z, Pu T, Degano M, et al. Modified nonlinear active disturbance rejection control for PMSM speed regulation with frequency domain analysis. IEEE Transactions on Power Electronics. 2023; 38(7):8126-8134. doi: 10.1109/TPEL.2023.3262519

[33] Xu Y, Zhang W, Huang Y, Zou J. Multisector three-phase PMSM drive system with low-frequency and high-frequency PWM noise. IEEE Journal of Emerging and Selected Topics in Power Electronics. 2021; 10(2):1639-1648. doi: 10.1109/JESTPE.2021.3059280

[34] Xu B, Zhang L, Ji W. Improved non-singular fast terminal sliding mode control with disturbance observer for PMSM drives. IEEE Transactions on Transportation Electrification. 2021; 7(4):2753-2762. doi: 10.1109/TTE.2021.3083925